Advanced Materials

ADVANCED MATERIALS
www.advmat.de

RESEARCH ARTICLE

Tellurium Sub-Oxides Infrared Phototransistors for Adaptive Super-Resolution Image Reconstruction

He Shao[1] | Yuxuan Zhang[1] | Weijun Wang[1] | Boxiang Gao[1] | Yi Shen[1] | Zenghui Wu[1] | Pengshan Xie[1] | Jiachi Liao[1] | Zhengxun Lai[2] | You Meng[2] | Zhuoran Wang[3] | Guozhen Shen[3] | Johnny C. Ho[1,4,5,6]

[1]Department of Materials Science and Engineering, City University of Hong Kong, Hong Kong SAR, China | [2]College of Semiconductors (College of Integrated Circuits), Hunan University, Changsha, China | [3]School of Integrated Circuits and Electronics, Beijing Institute of Technology, Beijing, China | [4]State Key Laboratory of Terahertz and Millimeter Waves, City University of Hong Kong, Hong Kong SAR, China | [5]Shenzhen Research Institute, City University of Hong Kong, Shenzhen, China | [6]Institute for Materials Chemistry and Engineering, Kyushu University, Fukuoka, Japan

Correspondence: You Meng (youmeng@hnu.edu.cn) | Guozhen Shen (gzshen@bit.edu.cn) | Johnny C. Ho (johnnyho@cityu.edu.hk)

Received: 26 October 2025 | **Revised:** 22 December 2025 | **Accepted:** 25 December 2025

Keywords: adaptive sensor| disordered film| infrared detection| luminescent dielectric layer| super-resolution reconstruction

ABSTRACT

Infrared (IR) detection using crystalline silicon or III-V compounds is commonly utilized but often challenged by bulkiness and inefficiency. With the development of autonomous driving and machine vision, there is a growing need for IR technology to incorporate compact neural architectures. In this study, IR-sensitive *p*-type disordered tellurium sub-oxides (TeO_x) thin films are deposited via an inorganic blending strategy. By integrating a luminescent dielectric layer, synergistic charge transfer and photon-induced secondary excitation endow TeO_x-based IR-visible adaptive sensors (IVAS) with broadband detection and memory capabilities. The IR-driven modulation of IVAS convolutional weights enables super-resolution image reconstruction even under suboptimal conditions. This IVAS-based system achieves a peak signal-to-noise ratio of 27.55 dB (compared to 26.85 dB conventionally), a structural similarity index measure of 0.94 (compared to 0.88 conventionally), and a 13.8% reduction in mean absolute error. These findings highlight TeO_x-based IVAS as a robust and adaptive solution for IR machine vision systems.

1 | Introduction

Current infrared (IR) detection technologies predominantly utilize photodiodes and phototransistors based on crystalline silicon or III–V compound semiconductors [1–3]. These well-established platforms are known for their high sensitivity and rapid response speeds, making them suitable for passive thermal imaging, stable performance under variable lighting conditions, and effective operation in optically challenging environments [4–7]. Despite their widespread use, these technologies face inherent limitations, particularly in the advanced fields, such as autonomous sensing, immersive visual computing, and spectrally adaptive machine vision [8]. Notably, their narrow spectral response, dependence on complex growth processes, and limited compatibility with standard silicon-based electronics present significant barriers to large-scale integration, on-chip processing, and the development of next-generation intelligent sensing systems [9–11].

To address these limitations, alternative materials with broadband IR sensitivity, simplified processing, and compatibility with silicon-based technologies are being actively explored [6, 12]. Among these, thin-film oxide semiconductors have attracted considerable interest due to their low-temperature processability, environmental stability, and suitability for large-area processing [13]. However, most oxide semiconductors have wide bandgaps (> 2 eV), limiting their IR photoresponse [14–17]. In this context, *p*-type tellurium oxide (TeO_x) emerges as a promising candidate. Its

tunable sub-1 eV optical bandgap, resulting from mixed oxidation states and disordered lattice structures, provides intrinsic IR sensitivity while maintaining the thermal and chemical stability [18, 19]. Furthermore, TeO_x is compatible with scalable, room-temperature vacuum deposition techniques, such as sputtering or thermal evaporation, enabling cost-effective and CMOS-compatible device fabrication [20, 21]. While recent advances have demonstrated high-performance *p*-type transistors based on structural engineering of TeO_x and broadband photodetection through heterojunction design, these approaches remain fundamentally confined to the conventional paradigm of single-mode photodetection or electronic switching [22, 23]. Furthermore, the development of TeO_x-based systems is hindered not only by an incomplete understanding of composition–structure–property relationships in disordered phases but also by the lack of architectures capable of integrating sensing, memory, and computational functions. Critically, the potential of TeO_x for constructing adaptive perception systems remains largely unexplored, leaving a significant gap between its device performance and applicability in intelligent machine vision.

In this work, we employ an inorganic blending strategy to fabricate *p*-type disordered TeO_x thin films, achieving intrinsic IR sensitivity and tunable electronic properties. Apart from material optimization, we have constructed an infrared-visible adaptive sensor (IVAS) through the integration of a luminescent dielectric layer, where synergistic charge transfer and cascaded secondary excitation enable broadband detection and memory functionality. Most significantly, the IR illumination serves as a dynamic control signal, enabling adaptive weight modulation for processing visible-light images. By directly converting IR signals into conductance changes, it implements a light control mechanism. This approach fundamentally simplifies the system architecture by merging the control and computing phases, thereby facilitating in-situ weight modulation. The efficacy of this IR-driven adaptation is validated through robust super-resolution (SR) image reconstruction under challenging lighting conditions. With IR-driven adaptive weight optimization enabled by IVAS, we achieve performance improvements, including a peak signal-to-noise ratio (PSNR) of 27.55 dB (compared to 26.85 dB conventionally), a structural similarity index measure (SSIM) of 0.94 (vs 0.88 conventionally), and a 13.8% reduction in mean absolute error (MAE).

2 | Results and Discussion

2.1 | SR Reconstruction Enabled by IVAS Array

To address the growing demands for adaptive sensing, we introduce an IVAS architecture that couples a *p*-type TeO_x thin-film with a luminescent dielectric layer. As shown in Figure 1a, the IVAS exhibits a dual-mode photoresponse, enabling broadband sensitivity across the visible and IR region. This wide spectral response arises from the synergistic interplay between interfacial charge transfer and photon-induced secondary excitation (Figure 1b). After that, the IVAS array is directly embedded into a super-resolution convolutional neural network (SRCNN) framework, functioning not only as a photodetector but also as a hardware-level memory unit (Figure 1c). Light-induced conductance modulation in the TeO_x channel can be retained and mapped to convolutional weights. Each IVAS pixel operates as a reconfigurable unit under IR illumination, where the corresponding conductance programming supports environmental adaptation (Figure 1d). This dynamic IR-driven weight modulation facilitates the network to adapt its parameters in response to challenging lighting (Figure 1e). As demonstrated in Figure 1f, conventional SRCNN fails to reconstruct image fidelity under low-light conditions [24]. In contrast, the IVAS-integrated system recovers key spatial features by leveraging IR-driven weight optimization (Figure 1g). This highlights the potential of IVAS as a foundational element in intelligent, environment-adaptive machine vision platforms.

2.2 | Characterizations of *p*-Type Disordered TeO_x Films

The IVAS device was fabricated using a *p*-type TeO_x channel and a luminescent dielectric layer, as confirmed by high-resolution scanning transmission electron microscopy (HR-STEM) and energy-dispersive X-ray spectroscopy (EDS) elemental mapping (Figure 2a). The TeO_x thin-film with a thickness of ~8 nm was deposited via room-temperature thermal evaporation (See the Methods section). The uniform and continuous TeO_x films were obtained using an inorganic blending strategy, exhibiting a smooth surface with a roughness of 0.32 nm (Figures S1 and S2). As shown in Figure 2b, it reveals that the $CsPbI_3$ perovskite quantum dots (PQDs) display distinct diffraction spots. In contrast, the TeO_x layer presents diffuse diffraction rings, confirming its disordered property. The characteristic vibrational modes of the helical chain structure in our TeO_x are revealed by Raman analysis, which shows three well-resolved peaks assigned to fundamental phonon modes (Figure 2c) [25]. Furthermore, X-ray photoelectron spectroscopy (XPS) verifies the simultaneous presence of both elemental Te^0 and oxidized Te^{4+} states (Figure 2d) [26–28].

During thermal evaporation, the oxygen content of TeO_x films can be precisely tuned by adjusting the Te/TeO_2 source ratio (Figure S3), enabling systematic investigation of structural characteristics across varying oxygen stoichiometries (x = 1.12, 1.60, and 2). X-ray diffraction (XRD) patterns of all compositions show the absence of diffraction peaks (Figure 2e; Figure S4), indicating that they maintain their disordered properties [20, 29, 30]. To further elucidate the amorphization mechanism, melt-quenching-based molecular dynamics (MD) simulations were performed (Figure 2f; Figure S5) [31, 32]. Radial distribution function (RDF) analysis reveals the retention of short-range Te—O bonding (~2 Å) in disordered TeO_x. At the same time, long-range order characteristic of the crystalline phase is suppressed (Figure 2g; Figure S6). These findings suggest that the structure preserves local coordination motifs and that disordering predominantly disrupts extended atomic networks [33, 34].

To elucidate the oxidation-state-dependent charge transport modulation, we conducted electrical characterization on TeO_x films (x = 1.12 and 1.60). The bare TeO_x (x = 1.12)-based transistor exhibited a field-effect mobility (μ_{FE}) of 3.80 $cm^2 \cdot V^{-1} \cdot s^{-1}$, while the TeO_x (x = 1.60) device showed a reduced μ_{FE} of 1.52 $cm^2 \cdot V^{-1} \cdot s^{-1}$ (Figure S7). This pronounced mobility disparity results from the introduction of higher oxygen levels. This process creates a

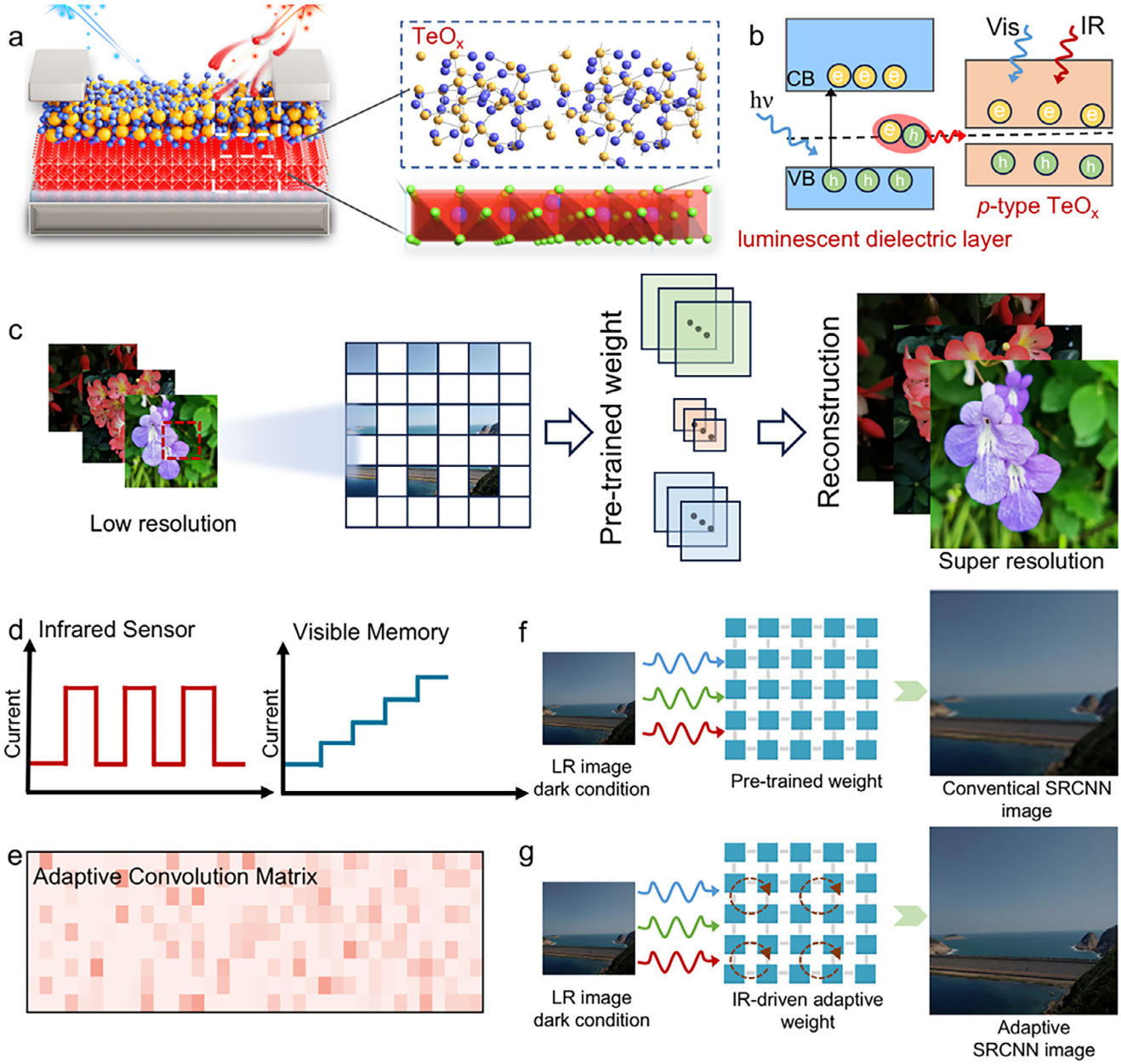

FIGURE 1 | (a) Structural schematic of the IVAS device, highlighting its broadband photodetection under visible and IR illumination. (b) Operational mechanism showing synergistic charge transfer and photon-induced secondary excitation. (c) Neural network architecture of SRCNN. (d) Dual-mode functionality of IVAS, enabling IR sensing and visible-light memory. (e) Adaptive weight mapping protocol within the SRCNN enabled by IR-driven modulation. (f) Conventional super-resolution under dark conditions (g) Enhanced image reconstruction achieved through IR-driven adaptive weight modulation in SRCNN. Photograph credits of 1c, 1f, and 1g: He Shao.

dense distribution of trap states and scattering centers, which in turn impede carrier transport [35, 36]. Despite its lower mobility, the TeO_x (x = 1.60) device displays an enhanced I_{on}/I_{off} ratio, attributable to improved carrier regulation at a cost of the reduced charge percolation [37, 38].

2.3 | Luminescent Dielectric Engineering of IVAS

After identifying TeO_x with balanced charge transport and switching characteristics, the TeO_x-based IVAS was subsequently fabricated by integrating with a luminescent dielectric layer. The luminescent dielectric layer consists of $CsPbI_3$ PQDs embedded in polystyrene (PS). The PQDs were synthesized via the hot-injection method (as illustrated in Figure S8), yielding a uniform size distribution and stable black-phase characteristics (Figures S9 and S10) [39, 40]. The luminescent dielectric layer mainly contributes to enhanced optoelectronic performance in visible regions while preserving the fundamental electronic characteristics of TeO_x films. As shown in Figures S11 and S12, the transfer and output characteristics exhibit typical *p*-type behavior, with an on/off ratio of 10^4 and a mobility of 2.5 $cm^2\ V^{-1}\ s^{-1}$. Furthermore, the influence of TeO_x film thickness on device behavior was explored (Figure S13), with statistical mobility and

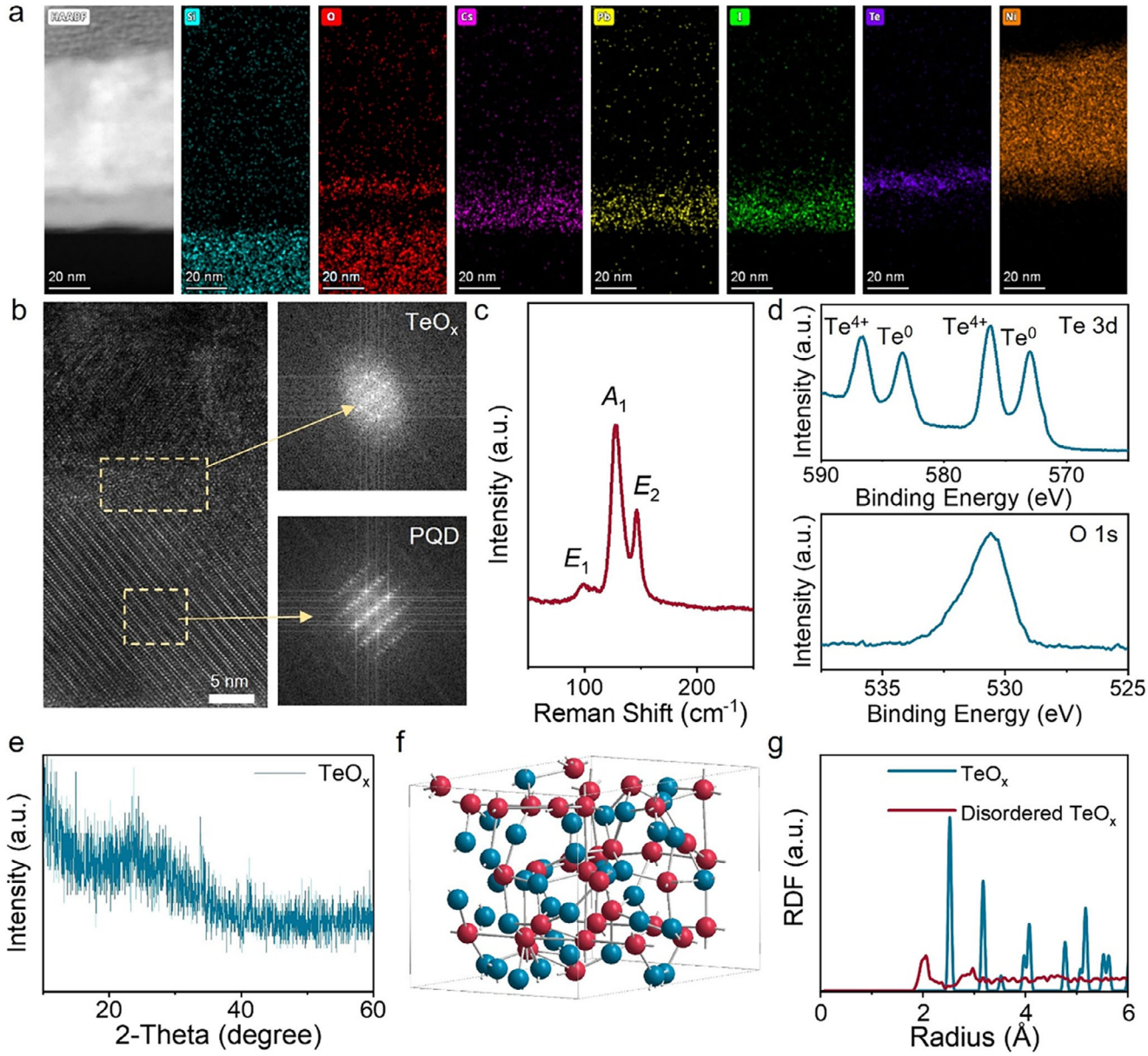

FIGURE 2 | (a) Cross-sectional HR-STEM image and corresponding EDS elemental mapping of the device. (b) HRTEM image showing the layered device architecture. (c) Reman spectra of the TeO_x film. (d) XPS of Te 3d and O 1s core levels of the TeO_x film. (e) The XRD pattern of the disordered TeO_x film. (f) Atomic structure of the disordered TeO_x. (g) RDFs of the disordered and crystalline TeO_x.

I_{on}/I_{off} summarized in Figure S14. These findings reveal that increasing the TeO_x film thickness beyond 10 nm results in higher off-state currents and a reduced on/off current ratio, due to the presence of excessive unoxidized Te [41]. Conversely, decreasing the thickness below 6 nm results in a significant reduction in mobility, primarily due to an insufficient carrier density.

To assess device uniformity and operational consistency, a 5 × 5 IVAS array was fabricated and characterized (Figure S15). Individual devices exhibited intense and persistent photocurrent responses under illumination at 450, 532, and 635 nm (Figure 3a) [42]. The current mapping across the array (Figure 3b; Figure S16) reveals uniform responsivity, confirming the reproducibility of the fabrication process. Under 100 consecutive light pulses (2 Hz), devices display robust and stable memory behavior across all tested wavelengths (Figure 3c), highlighting their capability for broadband optical memory. The memory mechanism in our devices is governed by complementary charge-trapping processes. The trapping state at the TeO_x/PQDs heterointerface enables the persistent photocurrent, while intrinsic defects within the PQDs and the surrounding PS matrix further contribute to charge retention [43–45]. In contrast, control devices comprising only TeO_x channels exhibited volatile behavior under identical conditions (Figure S17), underscoring the essential role of the dielectric layer in enabling persistent photocurrent memory.

To further elucidate the synergistic optical interactions within the hybrid structure, a cascaded secondary excitation mechanism is proposed and experimentally validated. As shown in Figure 3d, the photoluminescence (PL) spectrum of the luminescent layer exhibits a sharp emission peak centered at ~685 nm, with the inset

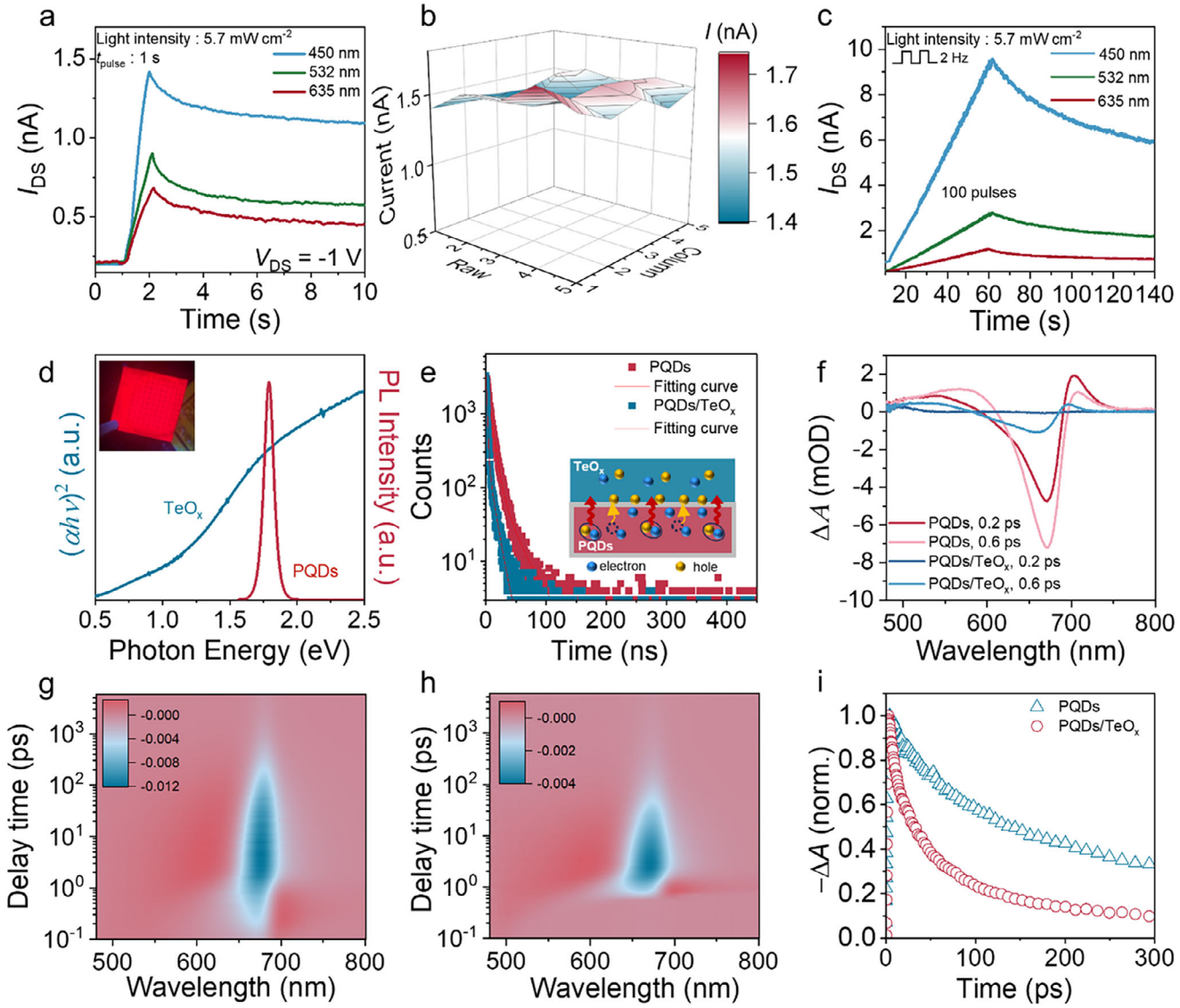

FIGURE 3 | (a) Photoresponse of IVAS under a single light pulse at 450, 532, and 635 nm (V_{DS} = −1 V and V_R = 5 V). (b) Spatial photocurrent distribution across the 5 × 5 IVAS array under 450 nm illumination. (c) Wavelength-dependent response under 100 consecutive light pulses. (d) Absorption spectrum of the TeO_x film and PL spectrum of the PQD film. Inset: IVAS array under 365 nm UV illumination. (e) TRPL of the PQD film and PQDs/TeO_x composite film. (f) TA of the PQD film and PQDs/TeO_x composite film at different delay times. The TA contour maps (ΔA–λ–time) of the (g) PQD film and (h) PQDs/TeO_x composite film under 450 nm excitation. (i) Decay dynamics at 670 nm (λ_{ex} = 450 nm).

photograph displaying red luminescence under optical excitation [46]. Concurrently, the TeO_x layer demonstrates strong optical absorption in the near-IR region, attributed to its narrow bandgap of approximately 0.8 eV. Critically, the emission spectra of the luminescent layer overlap substantially with the absorption edge of TeO_x, enabling the emitted photons to be reabsorbed by the TeO_x channel. This reabsorption triggers a secondary photoexcitation process within TeO_x. Thus, the observed memory behavior is also primarily governed by the synergistic interplay between cascaded photon recycling and efficient charge transfer at the heterointerface. Although alternative pathways such as trap-assisted tunneling and interface dipole effects were considered, the collective evidence most consistently supports this coupled mechanism as being responsible for the memory behavior.

Following this, PL and time-resolved PL (TRPL) measurements were conducted to investigate the charge transfer behavior. As shown in Figure S18, the TeO_x/PQDs composite film exhibits a significant reduction in photoluminescence (PL) intensity compared to the pristine PQD film. This fluorescence quenching is corroborated by the TRPL results in Figure 3e, which show a markedly shortened lifetime in the composite film [47, 48]. The observed simultaneous decrease in both PL intensity and lifetime provides strong evidence for the efficient charge transfer from the PQDs to the TeO_x layer [45, 49]. To gain further insights into the excited-state dynamics, femtosecond transient absorption (TA) spectroscopy was performed on both pristine and composite films under 450 nm excitation. The TA spectra at 0.2 and 0.6 ps delay (Figure 3f) show a pronounced ground-state bleaching

(GSB) centered near 670 nm, corresponding to the PQDs band edge. In pristine PQDs, a positive excited-state absorption (ESA) component emerges beyond 685 nm, which is notably suppressed in the PQDs/TeO_x composite structure.

The two-dimensional TA contour mappings (Figure 3g,h) further visualize the temporal evolution of this photo-induced evolution. Compared to the PQD film, the composite film shows an accelerated decay of both GSB and ESA signals, indicating faster carrier relaxation dynamics [50, 51]. The suppression of ESA in the composite film is particularly significant in the red region, implying that the emitted photons are reabsorbed by the broadband-absorbing TeO_x layer. To quantify the relaxation kinetics, the GSB decay traces at 670 nm were extracted (Figure 3i). The composite film exhibits a much shorter carrier lifetime than the pristine PQDs, in agreement with the TRPL results. The consistent trend in TRPL and TA confirms that the TeO_x layer serves as an energy extraction channel through radiative reabsorption.

2.4 | IR-Visible Synergistic Effect in IVAS Array

Beyond the visible light irradiation, the IVAS device exhibits pronounced sensitivity to IR illumination. As shown in Figure 4a,b, the photocurrent increases monotonically with increasing light intensity, highlighting the device's broadband and tunable optoelectronic response. The observation of a pronounced photoresponse in a bare TeO_x-transistor under 1550 nm irradiation confirms that the TeO_x layer itself is the primary site for IR detection (Figure S19). This is consistent with its intrinsically narrow bandgap (~0.8 eV) and pronounced Urbach tail, which provides localized states for efficient photon capture via phonon-assisted transitions. Furthermore, the precise voltage-dependent photocurrent modulation in the IVAS (Figure 4c) substantiates that direct photocarrier generation and control occur within the TeO_x layer, facilitating efficient photocurrent generation [52, 53].

To investigate the wavelength-selective modulation, sequential visible and IR irradiation were applied to the device (Figure S20). As shown in Figure 4d, under continuous 450 nm optical pulses at 0.1 Hz, the device exhibits distinct multi-level conductance states. During the intervals between pulses, stimulation with higher-frequency IR light induces discrete conductance levels. As shown in Figure 4e, a total of sixteen conductance states (4 bits) are uniformly distributed and exhibit an approximately linear relationship, which is critical for analog computing and dynamic weight mapping in neural networks. A statistical analysis of conductance modulation ratios under IR and visible illumination (σ/μ) reveals a pronounced initial-state-dependent response, suggesting a synergistic and programmable conductance tuning operation (Figure 4f). This dynamic persists under additional visible-light wavelengths (Figure S21), further validating the broadband feedback process.

The underlying mechanisms of IVAS under illumination are further clarified through an analysis of the energy band structure (Figure 4g,h). Absorption and UPS measurements (Figures S22 and S23) confirm the formation of a type-I heterojunction between PQDs and TeO_x, promoting directional carrier transport [54]. Upon visible-light exposure, both PQDs and TeO_x undergo excitonic dissociation, resulting in the generation of electron–hole pairs. The photogenerated holes in PQDs migrate into the TeO_x layer, while electrons remain trapped within the PQDs or at the interface, resulting in persistent charge accumulation and a memory effect. Moreover, photoluminescent emission from PQDs provides an additional energy recycling pathway, wherein the emitted red photons are reabsorbed by TeO_x through cascaded photon harvesting. Under 1550 nm illumination, photogenerated carriers in TeO_x exhibit rapid recombination, leading to a characteristic volatile photocurrent behavior. The synergy effect of visible-induced charge retention and IR-induced volatile photoresponse provides an adaptive optoelectronic platform.

2.5 | IR-Driven Adaptive Image SR Reconstruction

The IVAS architecture was further integrated with SRCNN to achieve simultaneous high-fidelity image reconstruction and enhanced feature extraction (Figure 5a) [55, 56]. The SRCNN framework was specifically selected for its architectural compatibility with our hardware implementation, where its constrained network depth and convolutional topology significantly relax the precision requirements for conductance control in the array (Figure S24). The super-resolution performance of the IVAS architecture was evaluated using a DIV2K dataset for training, with low-resolution inputs prepared for 2 × upscaling [24]. After training the SRCNN to obtain optimized weights, the learned parameters were mapped to the conductance states of our hardware array. Experimentally captured images were then used for testing. A systematic comparison was conducted between the software-based model and the IVAS-implemented counterpart to assess their respective reconstruction performance. As shown in Figure 5b, both software-based and IVAS-implemented SRCNNs achieve PSNR values exceeding 28 dB based on the pre-trained weights, confirming the preservation of structural integrity and detail.

To systematically evaluate the robustness of the IVAS architecture to luminance variations in super-resolution tasks, we conducted comparative experiments under both standard and reduced brightness conditions. The original images were processed to create a controlled low-light benchmark, with brightness reduced by 40% to simulate challenging imaging conditions (Figure 5c; Note S1). An SRCNN model was first pre-trained on normal-light images to obtain baseline weights (Figure 5d; Notes S2 and S3). Crucially, instead of creating multiple specialized models, we trained a unified system. It was achieved by jointly optimizing the baseline weights with a modulation network that learns to generate weight perturbations (ΔW) in response to IR illumination. The modulated weights $W_{\text{effective}} = W_{\text{base}} + \alpha \Delta W_{\text{IR}}$ are optimal for the current lighting condition. These modulated weights are integrated into all three convolutional layers of the SRCNN (Note S4), enabling dynamic feature extraction.

As illustrated in Figure 5e, for inputs with normal brightness, SRCNN achieves higher reconstruction quality compared to bicubic interpolation, particularly in edge clarity and detail retention. The PSNR values are confirmed to be 27.65 dB (bicubic) and 28.40 dB (SRCNN). Under low-light conditions,

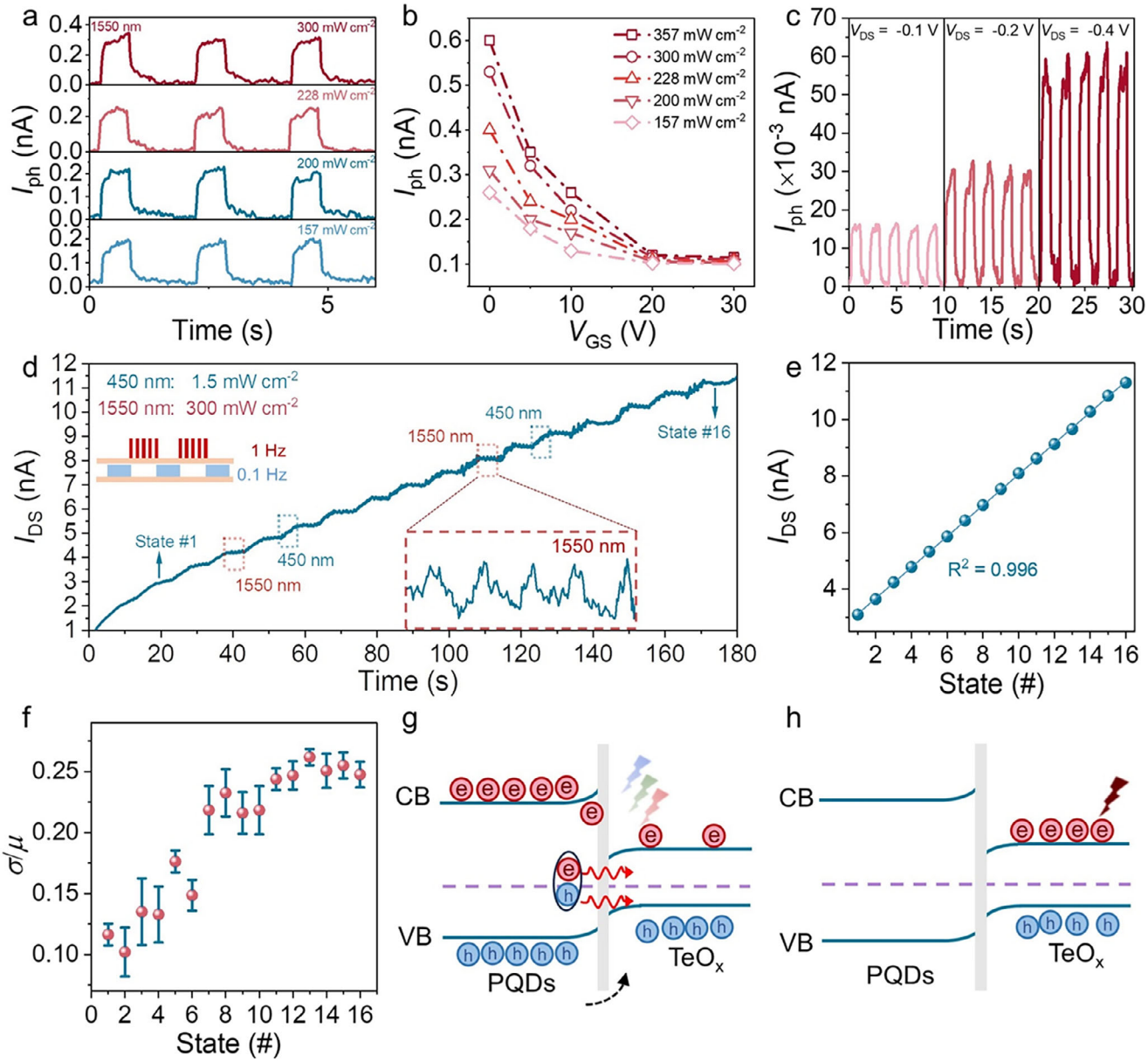

FIGURE 4 | (a) Photoresponse under 0.5 Hz switching with varying 1550 nm intensities (V_{DS} = - 1 V and V_R = 5 V). (b) Photocurrent of IVAS under 1550 nm light illumination as a function of gate voltage and light intensity. (c) Photoresponse with varying V_{DS}. (d) Multi-level conductance tuning by 450 nm pulses and 1550 nm pulses. (e) Linear fit between conductance state and pulse number. (f) Statistical analysis of photoconductance changes (σ: 1550 nm-induced variation; μ: per-pulse change for 450 nm) across sixteen conductance states. (g,h) Energy band evolution and charge carrier transfer process of IVAS under visible and IR illumination.

the conventional SRCNN with pre-trained weights exhibits significant performance degradation. In contrast, the fine-tuned model demonstrates marked improvements, benefiting from the IR-assisted functionality of the IVAS array. The PSNR improves from 26.85 to 27.55 dB, SSIM increases from 0.88 to 0.94, and MAE is reduced by 13.8%, indicating the array's ability to recover features in poorly illuminated scenes. Furthermore, the IVAS architecture leverages local conductance adaptation in different brightness environments to mitigate pixel saturation effects. As shown in Figure S25, these improvements highlight the array's capacity for preserving image details under undesirable lighting conditions.

3 | Conclusion

The proposed optoelectronic IVAS array, featuring IR-assisted adaptive weight modulation, offers a revolutionary approach to achieving efficient super-resolution imaging. By leveraging a *p*-type TeO_x channel layer coupled with a luminescent dielectric layer, the IVAS system dynamically adjusts convolutional weights to ensure robust feature extraction under diverse lighting conditions. The integration of IR modulation significantly enhances image reconstruction quality, as evidenced by an increase in PSNR from 26.85 to 27.55 dB, an improvement in SSIM from 0.88 to 0.94, and a 13.8% reduction in MAE compared to conventional

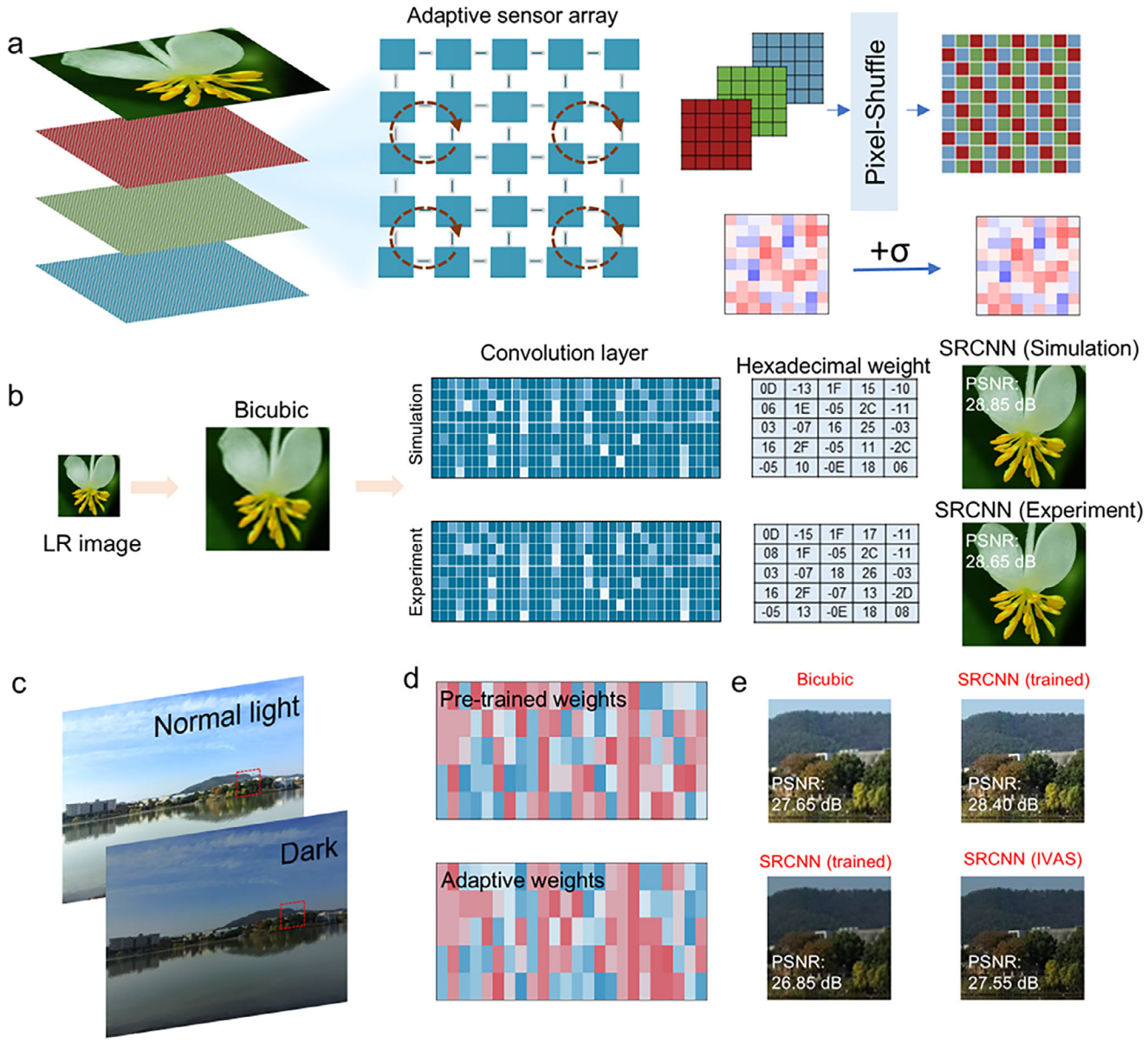

FIGURE 5 | (a) Schematic of the multimodal processing strategy of the IVAS array. (b) Performance comparison of HR image reconstruction between software-based and IVAS-based SRCNN. (c) Scene images under normal brightness and 40% brightness reduction. (d) Pre-trained SR weights (normal brightness) versus IR-driven weights under low-light conditions. (e) Bicubic versus SRCNN on normal-brightness images (top) and fixed pretrained weights versus adaptive weights on low-brightness images (bottom). Photograph credits of 5a, 5b, 5c, and 5e: He Shao.

SRCNN approaches. As the demand for intelligent and adaptive imaging systems increases, the IVAS approach presents a promising pathway to address these challenges, leveraging the strengths of advanced materials science and cutting-edge computational techniques.

4 | Experimental Section/Methods

4.1 | Measurement and Characterization

The optical properties of PQDs and TeO_x thin films were measured using Shimadzu UV-3600 and FLS-980 (Edinburgh Instruments). The femtosecond TAS was operated with the pump pulse of 450 nm, 150 fs, 1 kHz, and 100 μJ/cm^2. The morphologies of the TeO_x films were confirmed using AFM (Bruker Dimension Icon AFM) and SEM (Hitachi S3400N). The crystal structure of PQDs and TeO_x films was confirmed by XRD (D2 PHASER, Bruker). The chemical bonding and elemental composition were characterized by Raman spectroscopy (WITec RAMAN alpha 300R) and XPS measurements (Escalab 220i XL, VG Scientific). The structure and EDS mapping were examined using high-resolution transmission electron microscopy (HRTEM, Thermo Scientific, Talos F200X). The optoelectronic properties of the fabricated devices were evaluated using an Agilent 4155C semiconductor parameter analyzer combined with a precision probe station. For photodetector measurements, lasers with different wavelengths, including visible (450, 532, and 635 nm) and infrared (1550 nm), were used as light sources. The incident light powers (P) were determined using a power meter (PM400, Thorlabs).

4.2 | Device Fabrication

Bottom-gate top-contact thin-film transistors were fabricated on heavily doped *p*-type silicon substrates with 270 nm of thermally grown SiO_2. The fabrication process involved the following sequential steps: First, the SiO_2 surface was subjected to oxygen plasma treatment (5 min, 50 W) to enhance surface hydrophilicity and remove organic contaminants. Subsequently, 10 mg/mL PQDs solution in toluene was mixed with 6 mg/mL PS solution at a 1:1 volume ratio. The mixture was then spin-coated onto the substrate at 3000 rpm for 60 s. The synthesis process of $CsPbI_3$ PQDs was introduced in Figure S8. The deposition sources with controlled oxygen stoichiometry were synthesized through solid-state reactions between high-purity Te (99.999%) and TeO_2 (99.99%) powders, where the TeO_x (x = 1.12) composition was achieved using a 270:30 mg (9:1 molar ratio) Te/TeO_2 mixture and the TeO_x (x = 1.60) composition was prepared with a 250:50 mg (5:1 molar ratio) Te/TeO_2 mixture. The mixture was then deposited onto the substrate using thermal evaporation under high-vacuum conditions (base pressure < 4×10^{-6} Torr) at a controlled deposition rate of 0.8 Å/s. Film thickness was precisely monitored in situ using an INFICON SQC-310 deposition controller and a quartz crystal microbalance. Subsequently, the substrate was annealed in air at 100 °C for 30 min to stabilize its oxidation state. Both the active channel and source/drain electrodes were defined through shadow mask patterning to minimize gate leakage currents and ensure accurate electrical characterization. The device fabrication was completed by electron-beam evaporation of nickel source/drain electrodes through the shadow mask.

4.3 | DFT Calculation

All calculations are performed within the framework of density functional theory using the projector augmented plane-wave method, as implemented in the Vienna ab initio simulation package. The generalized gradient approximation proposed by Perdew, Burke, and Ernzerhof is selected for the exchange-correlation potential. The long-range van der Waals interaction is described by the DFT-D3 approach. For electronic structure calculations, a plane-wave cutoff energy of 420 eV was employed, and the Kohn–Sham equations were solved with an energy convergence criterion of 10^{-5} eV. Gamma-point sampling was used for the Brillouin zone integration in all calculations. The disordered amorphous TeO_x (x = 1.12) structures were generated through a melt-quenching protocol within the framework of ab initio molecular dynamics (AIMD). The initial atomic configurations were randomized by premelting at 5000 K for 1 ps, then melting at 1200 K for 5 ps and rapid quenching to 400 K with a cooling rate of -100 K/ps. Final structural relaxations were performed until atomic forces converged to less than 0.02 eV/Å.

Acknowledgements

This work is supported by a fellowship award from the Research Grants Council of the Hong Kong SAR, China (Project No. CRS_CityU101/24), the Innovation and Technology Fund (Project No. MHP/044/23) from the Innovation and Technology Commission of the Hong Kong SAR, China, the Science Technology and Innovation Committee of Shenzhen Municipality (Project No. JCYJ20807114910021), and Guangdong Basic and Applied Basic Research Fundation (Project No. 2024A1515011922).

Funding

Research Grants Council of the Hong Kong SAR, China (CRS_CityU101/24). Innovation and Technology Fund (MHP/044/23) from the Innovation and Technology Commission of the Hong Kong SAR, China. Science Technology and Innovation Committee of Shenzhen Municipality (JCYJ20230807114910021). Guangdong Basic and Applied Basic Research Fundation (2024A1515011922).

Conflicts of Interest

The authors declare no conflict of interest.

Data Availability Statement

The data that support the findings of this study are available from the corresponding author upon reasonable request.

References

1. Y. Yang, J. Seong, M. Choi, et al., "Integrated Metasurfaces for Re-Envisioning a Near-Future Disruptive Optical Platform," *Light: Science & Applications* 12 (2023): 152.

2. D. Chen, S. D. March, A. H. Jones, et al., "Photon-Trapping-Enhanced Avalanche Photodiodes for Mid-Infrared Applications," *Nature Photonics* 17 (2023): 594–600, https://doi.org/10.1038/s41566-023-01208-x.

3. W. Liu, J. Lv, L. Peng, et al., "Graphene Charge-Injection Photodetectors," *Nature Electronics* 5 (2022): 281–288, https://doi.org/10.1038/s41928-022-00755-5.

4. T. Xu, F. Zhong, P. Wang, et al., "Van der Waals Mid-Wavelength Infrared Detector Linear Array for Room Temperature Passive Imaging," *Science Advances* 10 (2024): adn0560, https://doi.org/10.1126/sciadv.adn0560.

5. M. Dai, C. Wang, B. Qiang, et al., "On-Chip Mid-Infrared Photothermoelectric Detectors for Full-Stokes Detection," *Nature Communications* 13 (2022): 4560, https://doi.org/10.1038/s41467-022-32309-w.

6. B. Ouyang, J. Wang, G. Zeng, et al., "Bioinspired In-Sensor Spectral Adaptation for Perceiving Spectrally Distinctive Features," *Nature Electronics* 7 (2024): 705–713, https://doi.org/10.1038/s41928-024-01208-x.

7. J. Guo, S. Gu, L. Lin, et al., "Type-Printable Photodetector Arrays for Multichannel Meta-Infrared Imaging," *Nature Communications* 15 (2024): 5193, https://doi.org/10.1038/s41467-024-49592-4.

8. S. T. Ha, Q. Li, J. K. Yang, H. V. Demir, M. L. Brongersma, and A. I. Kuznetsov, "Optoelectronic Metadevices," *Science* 386 (2024): adm7442, https://doi.org/10.1126/science.adm7442.

9. A. Morteza Najarian, M. Vafaie, A. Johnston, et al., "Sub-Millimetre Light Detection and Ranging Using Perovskites," *Nature Electronics* 5 (2022): 511–518, https://doi.org/10.1038/s41928-022-00799-7.

10. B. Kim, S. Y. Lee, H. Ko, et al., "Ultrahigh-Gain Colloidal Quantum Dot Infrared Avalanche Photodetectors," *Nature Nanotechnology* 20 (2025): 237–245, https://doi.org/10.1038/s41565-024-01831-x.

11. J. Wu, J. Zhang, R. Jiang, et al., "High-Sensitivity, High-Speed, Broadband Mid-Infrared Photodetector Enabled by a Van der Waals Heterostructure With a Vertical Transport Channel," *Nature Communications* 16 (2025): 564, https://doi.org/10.1038/s41467-025-55887-x.

12. H. Lu, J. Zhao, B. Zheng, C. Qian, T. Cai, E. Li, and H. Chen, "Eye Accommodation-Inspired Neuro-Metasurface Focusing," *Nature Communications* 14 (2023): 3301, https://doi.org/10.1038/s41467-023-39070-8.

13. E. Fortunato, P. Barquinha, and R. Martins, "Oxide Semiconductor Thin-Film Transistors: A Review of Recent Advances," *Advanced Materials* 24 (2012): 2945–2986, https://doi.org/10.1002/adma.201103228.

14. J. Shi, J. Zhang, L. Yang, M. Qu, D.-C. Qi, and K. H. L. Zhang, "Wide Bandgap Oxide Semiconductors: From Materials Physics to Optoelectronic Devices," *Advanced Materials* 33 (2021): 2006230, https://doi.org/10.1002/adma.202006230.

15. X. Yu, T. J. Marks, and A. Facchetti, "Metal Oxides for Optoelectronic Applications," *Nature Materials* 15 (2016): 383–396, https://doi.org/10.1038/nmat4599.

16. J. An, X. Zhao, Y. Zhang, et al., "Perspectives of 2D Materials for Optoelectronic Integration," *Advanced Functional Materials* 32 (2022): 2110119, https://doi.org/10.1002/adfm.202110119.

17. F. Teng, K. Hu, W. Ouyang, and X. Fang, "Photoelectric Detectors Based on Inorganic p-Type Semiconductor Materials," *Advanced Materials* 30 (2018): 1706262, https://doi.org/10.1002/adma.201706262.

18. Y. Meng, W. Wang, R. Fan, et al., "An Inorganic-Blended p-Type Semiconductor With Robust Electrical and Mechanical Properties," *Nature Communications* 15 (2024): 4440, https://doi.org/10.1038/s41467-024-48628-z.

19. Y. Zhang, J. Wang, P. Xie, et al., "Molecular Reconfiguration of Disordered Tellurium Oxide Transistors With Biomimetic Spectral Selectivity," *Advanced Materials* 36 (2024): 2412210, https://doi.org/10.1002/adma.202412210.

20. T. Kim, C. H. Choi, P. Byeon, et al., "Growth of High-Quality Semiconducting Tellurium Films for High-Performance p-Channel Field-Effect Transistors With Wafer-Scale Uniformity," *Npj 2D Materials and Applications* 6 (2022): 4, https://doi.org/10.1038/s41699-021-00280-7.

21. C. Zhao, H. Batiz, B. Yasar, W. Ji, M. C. Scott, D. C. Chrzan, and A. Javey, "Orientated Growth of Ultrathin Tellurium by van der Waals Epitaxy," *Advanced Materials Interfaces* 9 (2022): 2101540, https://doi.org/10.1002/admi.202101540.

22. S. Bang, C. Lee, D. Choi, et al., "High Performance P-Channel Transistor Based on Amorphous Tellurium Trioxide," *Advanced Materials* 37 (2025): 2504948, https://doi.org/10.1002/adma.202504948.

23. H. Xu, T. Kim, H. Han, et al., "High-Performance Broadband Phototransistor Based on TeO_x/IGTO Heterojunctions," *ACS Applied Materials & Interfaces* 14 (2022): 3008.

24. E. Agustsson and R. Timofte, "NTIRE 2017 Challenge on Single Image Super-Resolution: Dataset and Study," in *2017 IEEE Conf. on Computer Vision and Pattern Recognition Workshops (CVPRW)* (IEEE, 2017), 126–135, https://doi.org/10.1109/CVPRW.2017.150.

25. N. Dewan, V. Gupta, K. Sreenivas, and R. Katiyar, "Growth of Amorphous TeO_x ($2 \leq x \leq 3$) Thin Film by Radio Frequency Sputtering," *Journal of Applied Physics* 101 (2007): 084910.

26. H. Im, J. O. Oh, Y. Lee, et al., "Heterogeneous Integration of Complementary Field-Effect Transistors for High-Performance Micro LED Displays," *Advanced Materials* 37 (2024): 2408034.

27. R. Raghvender, A. Bouzid, S. Cadars, D. Hamani, P. Thomas, and O. Masson, "Structure of Amorphous TeO_2 Revisited: A Hybrid Functional ab initio Molecular Dynamics Study," *Physical Review B* 106 (2022): 174201, https://doi.org/10.1103/PhysRevB.106.174201.

28. C. Zhao, C. Tan, D.-H. Lien, et al., "Evaporated Tellurium Thin Films for p-Type Field-Effect Transistors and Circuits," *Nature Nanotechnology* 15 (2020): 53–58, https://doi.org/10.1038/s41565-019-0585-9.

29. S. Bates, G. Zografi, D. Engers, K. Morris, K. Crowley, and A. Newman, "Analysis of Amorphous and Nanocrystalline Solids From Their X-Ray Diffraction Patterns," *Pharmaceutical Research* 23 (2006): 2333–2349, https://doi.org/10.1007/s11095-006-9086-2.

30. B. Wu, X. Liu, P. Liu, et al., "Synthesis of Amorphous Metal Oxides via a Crystalline to Amorphous Phase Transition Strategy," *Nature Synthesis* 4 (2025): 370–379, https://doi.org/10.1038/s44160-024-00704-4.

31. R. Devanathan, L. R. Corrales, W. J. Weber, A. Chartier, and C. Meis, "Molecular Dynamics Simulation of Disordered Zircon," *Physical Review B* 69 (2004): 064115, https://doi.org/10.1103/PhysRevB.69.064115.

32. W. Luedtke and U. Landman, "Preparation and Melting of Amorphous Silicon by Molecular-Dynamics Simulations," *Physical Review B* 37 (1988): 4656, https://doi.org/10.1103/PhysRevB.37.4656.

33. J. Kang, X. Yang, Q. Hu, Z. Cai, L.-M. Liu, and L. Guo, "Recent Progress of Amorphous Nanomaterials," *Chemical Reviews* 123 (2023): 8859–8941, https://doi.org/10.1021/acs.chemrev.3c00229.

34. D. Sarkar, A. Bhui, I. Maria, M. Dutta, and K. Biswas, "Hidden Structures: A Driving Factor to Achieve Low Thermal Conductivity and High Thermoelectric Performance," *Chemical Society Reviews* 53 (2024): 6100–6149, https://doi.org/10.1039/D4CS00038B.

35. J. Lu, Y. He, C. Ma, et al., "Ultrabroadband Imaging Based on Wafer-Scale Tellurene," *Advanced Materials* 35 (2023): 2211562, https://doi.org/10.1002/adma.202211562.

36. P. Yang, J. Zha, G. Gao, et al., "Growth of Tellurium Nanobelts on h-BN for p-type Transistors With Ultrahigh Hole Mobility," *Nano-Micro Letters* 14 (2022): 109, https://doi.org/10.1007/s40820-022-00852-2.

37. J. Zheng, L. Ma, C. Li, R. Yuan, F. Chi, and Y. Guo, "on-State Current Paths and off-State Leakage in Nanoscale Silicene Field-Effect Transistors," *Physical Review Applied* 20 (2023): 014065, https://doi.org/10.1103/PhysRevApplied.20.014065.

38. A. Charnas, Z. Zhang, Z. Lin, et al., "Review—Extremely Thin Amorphous Indium Oxide Transistors," *Advanced Materials* 36 (2024): 2304044, https://doi.org/10.1002/adma.202304044.

39. J. Shi, F. Li, Y. Jin, et al., "In Situ Ligand Bonding Management of $CsPbI_3$ Perovskite Quantum Dots Enables High-Performance Photovoltaics and Red Light-Emitting Diodes," *Angewandte Chemie International Edition* 59 (2020): 22414–22421, https://doi.org/10.1002/anie.202010440.

40. Y.-F. Lan, J.-S. Yao, J.-N. Yang, et al., "Spectrally Stable and Efficient Pure Red $CsPbI_3$ Quantum Dot Light-Emitting Diodes Enabled by Sequential Ligand Post-Treatment Strategy," *Nano Letters* 21 (2021): 8756–8763, https://doi.org/10.1021/acs.nanolett.1c03011.

41. T. Kim, C. H. Choi, S. E. Kim, et al., "High-Performance Hexagonal Tellurium Thin-Film Transistor Using Tellurium Oxide as a Crystallization Retarder," *IEEE Electron Device Letters* 44 (2022): 269–272, https://doi.org/10.1109/LED.2022.3230705.

42. H. Shao, Y. Li, W. Yang, et al., "A Reconfigurable Optoelectronic Synaptic Transistor With Stable Zr-$CsPbI_3$ Nanocrystals for Visuomorphic Computing," *Advanced Materials* 35 (2023): 2208497, https://doi.org/10.1002/adma.202208497.

43. M. Hariharan and P. Kamat, "Tuning Excited-State Energy Transfer for Light Energy Conversion: A Virtual Issue," *ACS Energy Letters* 7 (2022): 2114–2117, https://doi.org/10.1021/acsenergylett.2c01167.

44. A. J. Nozik and J. Miller, "Introduction to Solar Photon Conversion," *Chemical Reviews* 110 (2010): 6443–6445, https://doi.org/10.1021/cr1003419.

45. Y. Wang, Z. Lv, J. Chen, et al., "Photonic Synapses Based on Inorganic Perovskite Quantum Dots for Neuromorphic Computing," *Advanced Materials* 30 (2018): 1802883, https://doi.org/10.1002/adma.201802883.

46. J. M. Richter, M. Abdi-Jalebi, A. Sadhanala, et al., "Enhancing Photoluminescence Yields in Lead Halide Perovskites by Photon Recycling and Light Out-Coupling," *Nature Communications* 7 (2016): 13941, https://doi.org/10.1038/ncomms13941.

47. C. de Weerd, L. Gomez, A. Capretti, et al., "Efficient Carrier Multiplication in $CsPbI_3$ Perovskite Nanocrystals," *Nature Communications* 9 (2018): 4199, https://doi.org/10.1038/s41467-018-06721-0.

48. M. Lu, X. Zhang, Y. Zhang, et al., "Simultaneous Strontium Doping and Chlorine Surface Passivation Improve Luminescence Intensity and Stability of $CsPbI_3$ Nanocrystals Enabling Efficient Light-Emitting Devices," *Advanced Materials* 30 (2018): 1804691, https://doi.org/10.1002/adma.201804691.

49. Y. Gao, Y. Yi, X. Wang, et al., "A Novel Hybrid-Layered Organic Phototransistor Enables Efficient Intermolecular Charge Transfer and

Carrier Transport for Ultrasensitive Photodetection," *Advanced Materials* 31 (2019): 1900763, https://doi.org/10.1002/adma.201900763.

50. J. Ma, T. J. Miao, and J. Tang, "Charge Carrier Dynamics and Reaction Intermediates in Heterogeneous Photocatalysis by Time-Resolved Spectroscopies," *Chemical Society Reviews* 51 (2022): 5777–5794, https://doi.org/10.1039/D1CS01164B.

51. C. Li, A. Wang, X. Deng, et al., "Insights Into Ultrafast Carrier Dynamics in Perovskite Thin Films and Solar Cells," *Acs Photonics* 7 (2020): 1893–1907, https://doi.org/10.1021/acsphotonics.0c00677.

52. S. Hao, M. Hetzl, V. F. Kunzelmann, et al., "Sub-Bandgap Optical Spectroscopy of Epitaxial β-Ga_2O_3 Thin Films," *Applied Physics Letters* 116 (2020): 092102, https://doi.org/10.1063/1.5143393.

53. V. M. Caselli, Z. Wei, M. M. Ackermans, E. M. Hutter, B. Ehrler, and T. J. Savenije, "Charge Carrier Dynamics Upon Sub-Bandgap Excitation in Methylammonium Lead Iodide Thin Films: Effects of Urbach Tail, Deep Defects, and Two-Photon Absorption," *ACS Energy Letters* 5 (2020): 3821–3827, https://doi.org/10.1021/acsenergylett.0c02067.

54. C.-C. Shih, Y.-C. Chiu, W.-Y. Lee, J.-Y. Chen, and W.-C. Chen, "Conjugated Polymer Nanoparticles as Nano Floating Gate Electrets for High Performance Nonvolatile Organic Transistor Memory Devices," *Advanced Functional Materials* 25 (2015): 1511–1519, https://doi.org/10.1002/adfm.201404329.

55. N. Aburaed, M. Q. Alkhatib, S. Marshall, J. Zabalza, and H. Al Ahmad, "3d Expansion of srcnn for Spatial Enhancement of Hyperspectral Remote Sensing Images," in *2021 4th Int. Conf. on Signal Processing and Information Security (ICSPIS)* (IEEE, 2021), https://doi.org/10.1109/ICSPIS53734.2021.9652420.

56. J. Zhang, J. Liu, and Z. Huang, "Improved Deep Learning Method for Accurate Flow Field Reconstruction From Sparse Data," *Ocean Engineering* 280 (2023): 114902, https://doi.org/10.1016/j.oceaneng.2023.114902.

Supporting Information

Additional supporting information can be found online in the Supporting Information section.

Supporting file: adma72046-sup-0001-SuppMat.docx